ChemPhysChem

Research Article
doi.org/10.1002/cphc.202400603

Chemistry Europe
European Chemical Societies Publishing

www.chemphyschem.org

On the supramolecular interactions into a pH- and Metal-Actuated Molecular Shuttle: some insights from QTAIM modeling

Costantino Zazza,*[a] Nico Sanna,[a, b] Stefano Borocci,[a, c] and Felice Grandinetti[a, c]

Supramolecular contacts responsible for chemical interaction of cucurbit[7]uril (**CB[7]**) macrocycle on a Tolyl-Viologen-Phenylene-Imidazole (**T-VPI**) molecular thread, at acid pH (**T-VPI-H$^+$**) or after Ag^+ cation addition (**T-VPI-Ag$^+$**), are analytically addressed in a computational framework combining Quantum Theory of Atoms in Molecules (QTAIM) with Density Functional Theory (DFT). In this respect, the crystallographic structure (CCDC number 2217466) is taken as reference condition for addressing the nature of the chemical interactions driving the shuttling of the **CB[7]** between **T** and **P** stations recently observed in dilute water solutions. Beside the host(**CB-[7]**) *vs* guest(**T-VPI-H$^+$** or **T-VPI-Ag$^+$**) complexation, the coordination sphere of the Ag^+ cation is also investigated by means of local electronic energy density - $H(\mathbf{r})$ - descriptors. The derived non-covalent interaction patterns are found to support diagnostic ^{1}H NMR signals used for detecting the mutual position of the **CB[7]** along the axle. This work highlights the potentialities of a QTAIM based approach in the characterization of supramolecular and metal-complexation effects in molecular aggregates such as not-interlocked synthetic molecular shuttles.

1. Introduction

Supramolecular systems are obtained by the association of two or more molecules, taking advantage of the so-called molecular recognition process based on mutual and specific interactions at nanoscale level.[1] In recent decades, we have witnessed the release of a myriad of synthetic systems resembling supramolecular systems already present in nature and capable of converting external stimuli or chemical signals into controlled molecular movements.[2–4] Therefore, using synthetic methods it is possible to assemble molecular aggregates that do not have elements of spontaneous recognition, but which can be appealing to associate for specific purposes.[5–7] In this respect, the design of molecular systems held together by supramolecular forces must necessarily include the use of molecular components having a very precise chemical and physical properties.[8–11] According to various type of needs and with the advances in miniaturization techniques we have observed the appearance molecular machines and devices with sizes even confined within single molecular aggregates.[12,13] The logic followed is that of promoting controllable directional motions, at molecular-size level, converting chemical energy or external stimuli (chemical reactions, pH-variation, electrochemical potential, UV–Vis radiation) in a way resembling the behaviour of macroscopic machines.[14–24] Artificial molecular machines operating in different environments have therefore emerged in the literature, including molecular switches, catenanes, motors, rotors and shuttles.[25] Ring shuttling processes since from their discovery in the early 1990s results particularly intriguing for the design of nano-technologically advanced smart materials based on soft matters.[26,27] Molecular shuttles are characterized by a macrocycle (MAC) hosting a molecular thread featuring different recognition sites termed as preferential "stations" for the MAC itself. Molecular shuttles can be classified into two different slots: *i)* the stimuli-responsive ones in which the ring translocation among different stations along an axle is activated by an external stimulus; *ii)* the spontaneous counterpart in which the ring shuttling occurs autonomously between near degenerate sites having similar affinities with the MAC. In this fascinating research area, Kriat et. al.[28] recently reported to the scientific community an aqueous pH- and Metal-actuated molecular shuttle in which the reversible coexistence of translational isomers is modulated by acidic conditions or by a gradual ratio of Ag^+ cations. More specifically, a cucurbit[7]uril (**CB[7]**) macrocycle on a Tolyl-Viologen-Phenylene-Imidazole (**T-VPI**) molecular wire, at acid pH (**T-VPI-H$^+$**) or after Ag^+ addition (**T-VPI-Ag$^+$**) is able to reversibly complex the **T** and **P** functional groups contrary to

[a] C. Zazza, N. Sanna, S. Borocci, F. Grandinetti
Department for Innovation in Biological, Agro-Food and Forest systems, Università della Tuscia (DIBAF), L.go dell'Università, s.n.c., Viterbo 01100, Italy
E-mail: costantino.zazza@unitus.it

[b] N. Sanna
CNR-ISTP (Istituto per la Scienza e Tecnologia dei Plasmi), Via G. Amendola 122/D, 70126 Bari, Italy

[c] S. Borocci, F. Grandinetti
Istituto per i Sistemi Biologici del CNR (ISB), Sede di Roma - Meccanismi di Reazione c/o Dipartimento di Chimica, Sapienza Università di Roma, P.le A. Moro 5, 00185 Rome, Italy

Supporting information for this article is available on the WWW under https://doi.org/10.1002/cphc.202400603

what had been observed on similar systems (see Scheme 1).[29] Given these surprising results which still remain difficult to explain with particular reference to the preferential interaction between the **CB[7]** and the **T** station, we therefore decided to investigate - for the first time - the supramolecular contacts between these functional units via the Quantum Theory of Atoms in Molecules (QTAIM)[30] computational framework. DFT methods[31] were performed at the theoretical level of B3LYP(D3)/cc-pVTZ in conjunction with Bader's topology analysis[30] and conceptual-DFT descriptors to obtain detailed information regarding the interaction of **CB[7]** with **T** and **P** stations. To this end, we focused our attention on the recently deposited crystallographic structure (CCDC:2217466)[28] featuring a host(**CB[7]**):guest(**T-VPI-Ag$^+$**) ratio equal to 2:1. In such a composition, the single-crystal structure unequivocally shows the presence of the MAC over both the aforementioned sites with the silver cation close to the imidazole function of the guest species.

2. Methods

Single crystals (CCDC:2217466)[28] of the host:guest 2:1 complex were taken as input coordinates within our simulation environment. In this context, the theoretical level employed in this study was the DFT[31] adopting the hybrid exchange-correlation Becke 3-parameters Lee–Yang–Parr (B3LYP) functional[32] -belonging to the class of generalized gradient approximation (GGA) functionals for the exchange-correlation energy[31] - in conjunction with the cc-pVTZ (henceforth denoted as VTZ) basis set.[33] In addition, we used Grimme's dispersion correction as an add-on to standard Kohn–Sham (KS) equations with the original D3 damping function (i.e., DFT–D3) as proposed in Ref. [34]; the total energy of the system ($E_{DFT\text{-}D3}$) is given by the usual self-consistent KS energy ($E_{KS\text{-}DFT}$) as obtained from the chosen functional with a correction for the dispersion correction as a sum of two- and three-body terms ($E_{disp}=E^{(2)}+E^{(3)}$). The two-body and three-body dispersion coefficients are derived *ab-initio* employing the well-known Casimir–Polder formula and the Axilrod–Teller–Muto term as estimated from the third-order perturbation theory for triples of atoms.[34] In this context, we would like to clarify that we considered, at DFT level, the two limit cases proposed in literature[28] in which the **CB[7]** firstly encircles the **T** station and then **P** one. The bonding analysis was accomplished using the Bader's theory of atoms in molecules (QTAIM).[30] The analyzed DFT-based indicators include the electron density $\rho(\boldsymbol{r})$, the electronic energy density $H(\boldsymbol{r})$ and its kinetic and potential components $G(\boldsymbol{r})$ and $V(\boldsymbol{r})$, respectively and the Reduced Density Gradient (RDG) $s(\boldsymbol{r})$. The $\rho(\boldsymbol{r})$ is defined, as usual, by the equation:

$$\rho(\boldsymbol{r}) = \sum_i \eta_i |\varphi_i(\boldsymbol{r})|^2 \tag{1}$$

where η_i is the occupation number of the natural orbital φ_i, in turn expanded as a linear combination of the atomic basis functions.[30] The $H(\boldsymbol{r})$ is the sum of the kinetic energy density $G(\boldsymbol{r})$ and the potential energy density $V(\boldsymbol{r})$:

$$H(\boldsymbol{r}) = G(\boldsymbol{r}) + V(\boldsymbol{r}) \tag{2}$$

The presently-employed definition[30,35] of the $G(\boldsymbol{r})$ is given by the equation:

$$G(\boldsymbol{r}) = \frac{1}{2}\sum_{i=1} \eta_i |\nabla\varphi_i(\boldsymbol{r})|^2 \tag{3}$$

with the sum running over all the occupied natural orbitals φ_i of occupation numbers η_i. The potential energy density $V(\boldsymbol{r})$ is evaluated[30] from the local form of the virial theorem:

$$V(\boldsymbol{r}) = \frac{1}{4}\nabla^2\rho(\boldsymbol{r}) - 2G(\boldsymbol{r}) \tag{4}$$

The RDG - coming from the density and its first derivative - is defined by the following equation[36]:

$$s(\boldsymbol{r}) = \frac{|\nabla\rho(\boldsymbol{r})|}{2(3\pi^2)^{\frac{1}{3}} \times \rho(\boldsymbol{r})^{\frac{4}{3}}} \tag{5}$$

Low-value of $s(\boldsymbol{r})$ isosurfaces (typically 0.3–0.6) appear among atoms undergoing any type of interaction, the Non-Covalent Interactions (NCIs) emerging, in particular, by considering the spatial regions of low $\rho(\boldsymbol{r})$ (typically at around 0.05 $e{\cdot}a_0^{-3}$). The low-$s(\boldsymbol{r})$/low-$\rho(\boldsymbol{r})$ isosurfaces are, in turn, mapped in terms of the $sign(\lambda_2){\times}\rho(\boldsymbol{r})$, λ_2 being the second eigenvalue ($\lambda_1 < \lambda_2 < \lambda_3$) of the Hessian matrix of $\rho(\boldsymbol{r})$. In essence, the sign of λ_2 is used to distinguish between attractive ($\lambda_2 < 0$) and repulsive ($\lambda_2 > 0$) interactions, and the value of $\rho(\boldsymbol{r})$ is exploited to rank the corresponding strength. Thus, the NCIs are conveniently visualized in a 2D plane by plotting the RDG *vs* the colored $sign(\lambda_2){\times}\rho(\boldsymbol{r})$, and in 3D space by plotting a chosen low-value isosurface of the $s(\boldsymbol{r})$, colored by the $sign(\lambda_2){\times}\rho(\boldsymbol{r})$ (standard employed colors range from blue to red for highly attractive to repulsive interactions, respectively). The analysis was done with the Multiwfn program (version 3.8.dev)[37] using the wfx files generated by the Gaussian 16 code (Rev. C01).[38] The 2D and 3D plots of the $s(\boldsymbol{r})$ *vs* $sign(\lambda_2){\times}\rho(\boldsymbol{r})$ were produced with

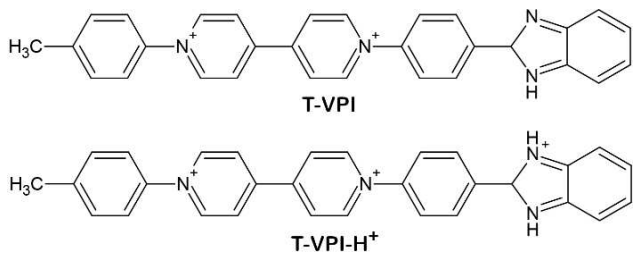

Scheme 1. Molecular structure of **T-VPI** and **T-VPI-H$^+$** functionalized molecular threads interacting with the **C**ucur**B**it[**7**]uril macrocycle (**CB**[**7**]) in aqueous environment. The systems are composed of 4 different groups (from left to right): Tolyl (**T**), Viologen (**V**), Phenylene (**P**) and Imidazole (**I** or **I-H$^+$**). The **T-VPI-Ag$^+$** species is formed starting from a dilute solution of **T-VPI** to which a solution of $AgNO_3$ is added. The Ag^+ cation behaves like a proton by coordinating to the nitrogen atom of the imidazole group.[28]

Atomistica.online[39] and the Visual Molecular Dynamics (VMD) program[40] setting $sign(\lambda_2)\times\rho(r)$ between -0.050 $e{\cdot}a_0^{-3}$ (blue) and 0.010 $e{\cdot}a_0^{-3}$ (red). Due to the reduced computational cost, DFT calculations are recommended over wavefunction-based post-SCF methods for practical visualization of noncovalent interactions in large molecular systems like the present ones.[36] We also analyzed the molecular Electrostatic Potential (ESP) surfaces - within the Libreta algorithm[41] - considering the molecular thread in two different forms (i.e., **T-VPI** and **T-VPI-H$^+$**) and the **CB[7]** macrocycle. Finally, solvation effects are considered by using the popular Conductor-like Polarizable Continuum Model (C-PCM).[42]

3. Results and Discussion

3.1. Identifying Noncovalent Interactions in CB[7]:T-VPI-H$^+$ Host:Guest Complex

At first, the ESP of the molecular thread in its neutral and protonated form were calculated at C-PCM/B3LYP(D3)/VTZ theoretical level after geometry optimization and using the Libreta algorithm[41] provided in Multiwfn software. Electrophilic sub-units in aqueous environment are represented by red color indicating negative regions of the molecule and are located – as it would have been expected - on more electronegative atoms or where lone pairs are located. Positive portions (blue color) instead correspond to nucleophilic regions suggesting – on average - a lack of electrons. For the neutral species, i.e., **T-VPI**, the ESP surface reflects the peculiar electrophilic *vs* nucleophilic character of the imposed "stations". The imidazole-based station features a high potential energy region located around the N–H group which makes this position prone of following a nucleophilic complexation with the macrocycle. On the contrary, the remaining part of this functional group presents negative values reflecting a potential electrophilic reactivity. The viologen moiety with two net positive charges show a widespread positive region of the ESP therefore sensitive to a nucleophilic complexation with the negative counterpart localized on the oxygen atoms in the carbonyl groups of the **CB[7]** macrocycle (see Figure 1). Afterwards we tested the influence of an acid solution of **T-VPI** introducing a proton on the nitrogen atom of the imidazole group. As a result, the **T-VPI-H$^+$** thread presents three positive electrostatic charges and a positive ESP map substantially distributed over the entire molecular structure. The observed trend unequivocally reveals that, in acidic conditions, all four functional groups can be attractive for a nucleophilic-driven complexation by the macrocycle. This picture results in line with the observed NMR data[28] suggesting – under acidic conditions - a reversible shuttling of the macrocycle between at least two stations along the **T-VPI-H$^+$** thread. In summary, this characterization of **T-VPI** and **T-VPI-H$^+$** in terms of electron-rich and -deficient regions provides a self-consistent prediction at DFT level about the potentially relevant interaction moieties with the encircling **CB[7]**.

As a next step, we started addressing – for the first time - the nature of van der Waals interactions, hydrogen bonds, and steric repulsion characterizing the supramolecular assembly observed in the X-ray structure of the host:guest 2:1 complex. Given the dimension of the overall complex, we decided to split out such a system in two molecular aggregates: a first aggregate composed by the **T-VPI-H$^+$** thread interacting with a single **CB[7]** fixed on the **T** station (where starting from X-ray coordinates we replaced the silver cation with a proton bound to the imidazole N atom); a second aggregate characterized by the presence of the **CB[7]** over the **P** station in the **T-VPI-Ag$^+$** thread (in this second subsystem we also considered the ordered water molecules detected in the coordination sphere of the Ag^+). These two investigated supramolecular systems are explicitly shown on the upper panel of Figure 2. The nature of the host:guest contacts in the first selected aggregate was

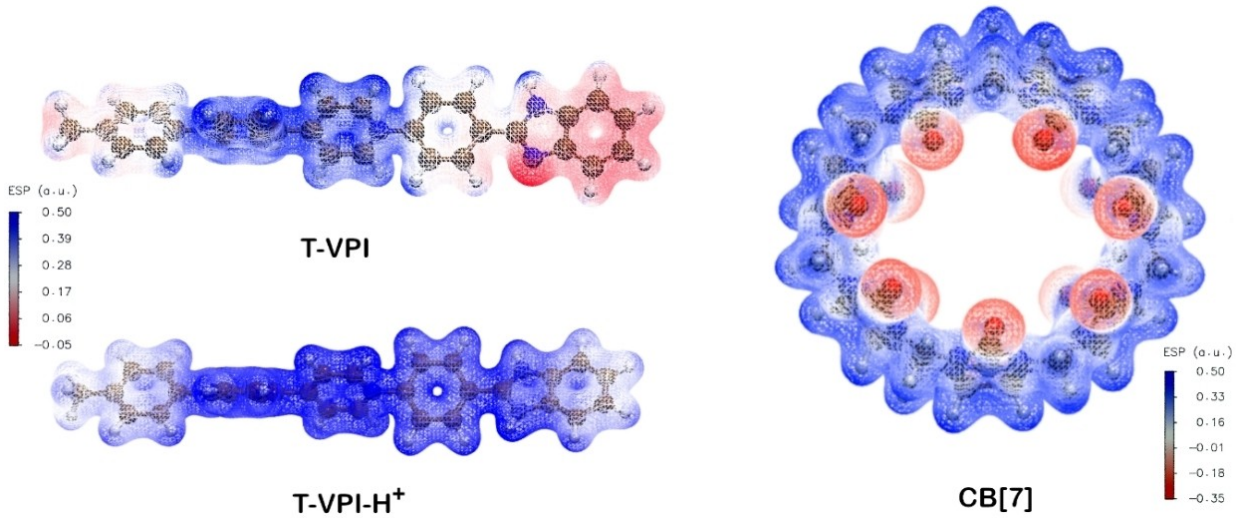

Figure 1. Electrostatic potential (ESP) colored electron density isosurface (isodensity value of 0.03 a.u.) for the **T-VPI**, **T-VPI-H$^+$** and **CB[7]** molecular systems in aqueous environment at C-PCM/B3LYP(D3)/VTZ level of theory; the colour scale bar is also shown.

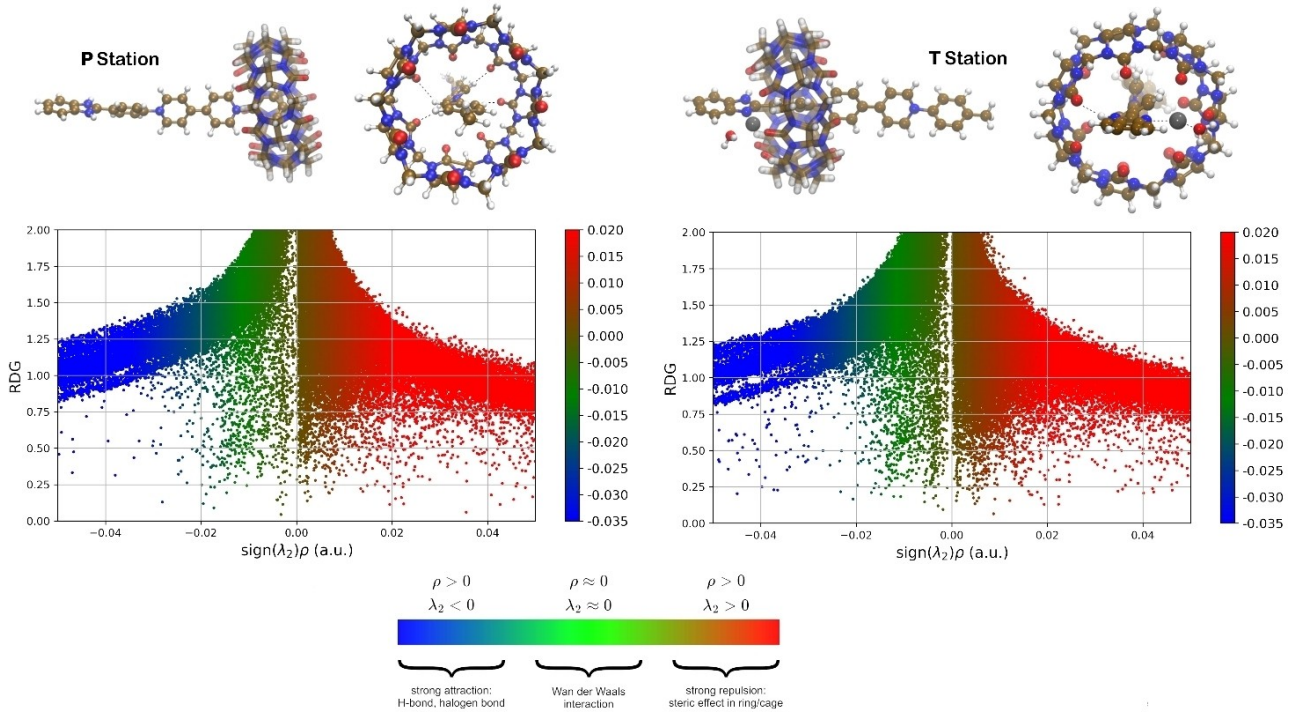

Figure 2. upper panel: molecular structure of the two investigated supramolecular aggregates starting from X-ray coordinates (see section 3.1); lower panel: the related 2D Reduced Density Gradient (RDG) plots in which the color bar represents the $sign(\lambda_2)\times\rho(r)$ in atomic units.

assayed by an RDG analysis and the relevant results are given in Figure 2 (left panel), Figure 3 and summarized in Table 1. For a direct comparison, in the right panel of Figure 2 we also report the RDG plot of the other investigated aggregate (i.e., **T-VPI(:CB[7]:)-Ag$^+$**) featuring the macrocycle encircling the **P** station with the contextual presence of a silver cation and a water

Table 1. Electron density $\rho(r)$ ($e{\cdot}a_0^{-3}$), Laplacian of electron density $\nabla^2\rho(r)$ ($e{\cdot}a_0^{-5}$), electron kinetic energy density $G(r)$ (hartree$\cdot a_0^{-3}$), electron potential energy density $V(r)$ (hartree$\cdot a_0^{-3}$), and electron energy density $H(r)$ (hartree$\cdot a_0^{-3}$) for bond critical points on selected bonds of the **CB[7]:T-VPI-H$^+$** molecular shuttle calculated at B3LYP(D3)/VTZ level of theory from the crystallographic structure (CCDC number 2217466).[28]

BCP[a]	Distance (in Å)	$\rho(r)$	$\nabla^2\rho(r)$	$G(r)$	$V(r)$	$-G(r)/V(r)$	$H(r)$
199[H37-O74]	3.45	0.001030	0.004889	0.000812	−0.000402	2.0199	0.00041
204[H37-O110]	2.58	0.007378	0.024171	0.005471	−0.004899	1.116759	0.000572
211[H38-O73]	3.88	0.000302	0.001703	0.000259	−0.000094	2.755319	0.000165
232[H38-O61]	4.34	0.000093	0.000667	0.000103	−0.000040	2.575	0.000063
255[H38-O60]	4.37	0.000081	0.000477	0.000069	−0.000019	3.631579	0.00005
237[H36-O146]	2.72	0.005284	0.019317	0.004082	−0.003335	1.223988	0.000747
258[H36-O84]	3.48	0.001028	0.004643	0.000754	−0.000348	2.166667	0.000406
230[H56-N69]	3.17	0.002871	0.009987	0.001956	−0.001415	1.382332	0.000541
327 [H53-N144]	2.91	0.004919	0.014794	0.003226	−0.002753	1.171813	0.000473
356[H53-N143]	3.01	0.003948	0.014515	0.002943	−0.002258	1.303366	0.000685
386[C50-O105]	3.13	0.003482	0.013315	0.002493	−0.001658	1.503619	0.000835
405[H51-O85]	2.26	0.014728	0.039283	0.010046	−0.0102704	0.978151	−0.000220
331[H58-O182]	2.59	0.008029	0.029017	0.006230	−0.005205	1.196926	0.001025
339[H58-O114]	2.84	0.004327	0.015770	0.003237	−0.002532	1.278436	0.000705
366[H24-O182]	2.49	0.007820	0.025424	0.005845	−0.005335	1.095595	0.000510
373[H24-O184]	3.22	0.001424	0.006994	0.001199	−0.000651	1.841782	0.000548
422[H13-O72]	2.12	0.017438	0.053825	0.012838	−0.012220	1.050573	0.000618

[a] BCP: from 199 to 339 involve the Tolyl (**T**) station in interaction with the **CB[7]**; from 366 to 422 the half unit of the Viologen (**V**) group, covalently bonded to **T**, in supramolecular contact with the **CB[7]**.

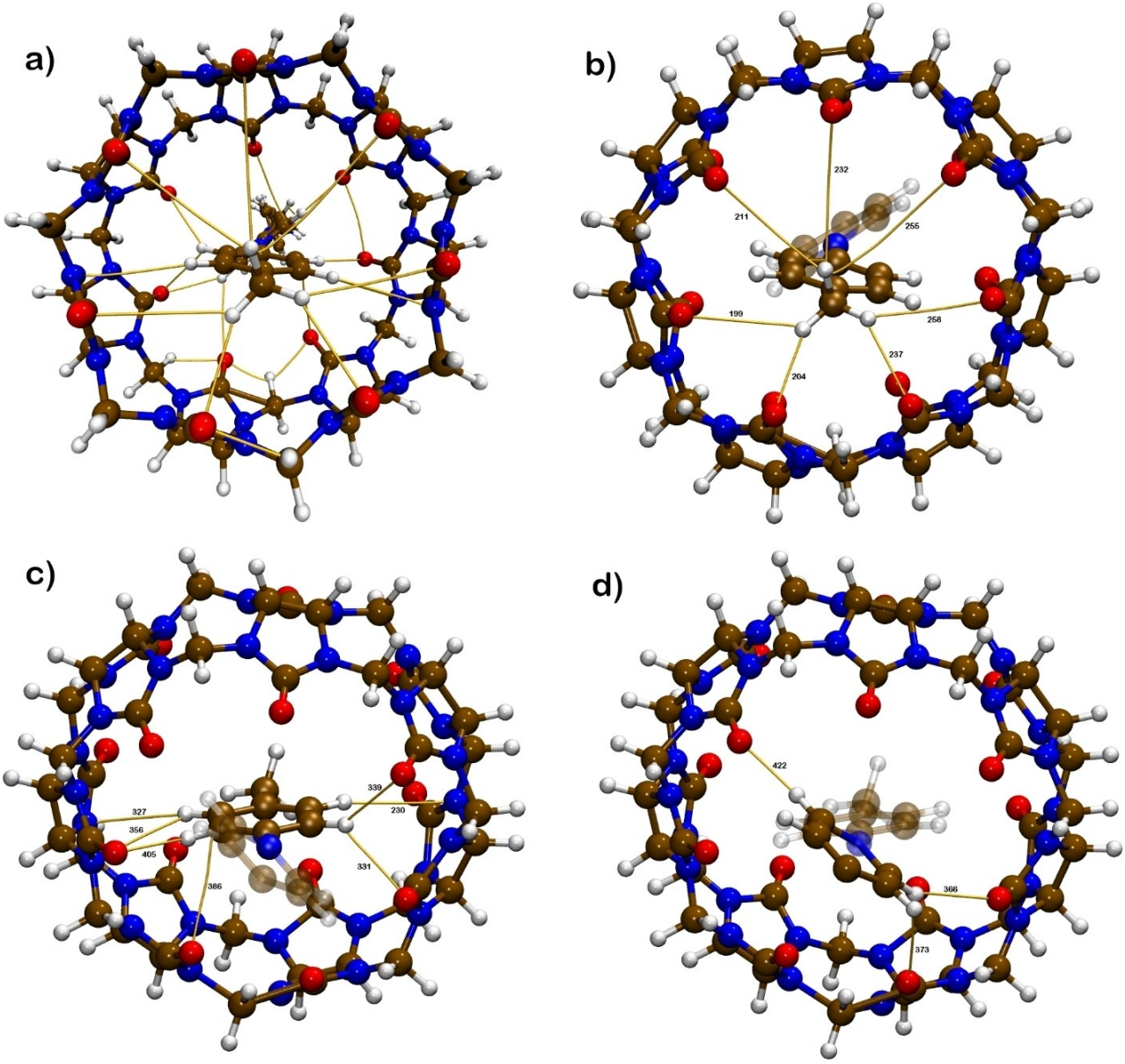

Figure 3. a) Non covalent bond paths – at B3LYP(D3)/VTZ level of theory – for the **CB[7]:T-VPI-H$^+$** molecular shuttle starting from X-ray crystallographic structure; bond paths connecting the **CB[7]** with the terminal methyl group of the **T** station (b), the aromatic ring of the **T** station (c) and the portion of the **V** station covalently bound with **T** (d). The labels used for identifying the bond paths within the AIM workflow are those reported in Table 1.

molecule. In this regard, the presence of these last two species increases the number of attractive supramolecular contacts compared to the situation derived by considering the macrocycle on the **T** station; the 2D plots of the RDG *vs sign*(λ_2)×ρ(*r*) in Figure 2 (lower panel), show non-covalent attractive contacts signaled by the AIM analysis as a broad distribution in the range of *sign*(λ_2)×ρ(*r*) between 0 and −0.05 $e{\cdot}a_0^{-3}$, colored as typical for van der Waals interactions. As for the **T-VPI(:CB[7]:)-Ag$^+$** system, this distribution suggests a system slightly more populated by intermolecular interactions as a result of a larger number of interacting species. A more punctual analysis of the non-covalent interaction patterns in the **CB[7]:T-VPI-H$^+$** system is depicted in Table 1. The region between the molecular thread and the macrocycle includes numerous ρ(***r***) Bond Critical Points (BCPs) of the type (+3,−1). A "critical point" (CP) in the electron density is a point in space at which the first derivatives of the density vanish (i.e., $\nabla\rho(\boldsymbol{r})=\boldsymbol{0}$, where the zero vector signifies that each individual derivative in the gradient operator, ∇, is zero and not just their sum). In this table we also report: *i)* the trace of the Hessian of the density known as the Laplacian of the density [$\nabla^2\rho(\boldsymbol{r})$]; this parameter allows an analysis of the curvatures of the ρ(***r***) at any estimated BCPs along the principal axes. *ii)* the analytical values of the *G*(***r***) and *V*(**r**) to compare the kinetic and potential energy densities; this to appreciate if interactions are dominated by a local reduction of the potential energy or by a local excess in the kinetic energy [we always have *G*(***r***)>0 and *V*(***r***)<0]. *iii)* The total energy density -see Equation (2) - which reflects a negative value for interactions

with significant sharing of electrons, so to reveal the covalent or partially covalent character of the interactions themselves. In this respect, Figure 3a summarizes the BCPs belong to Bond Paths (BPs) connecting different subunits in the investigated system; panel b) and c) in the same figure highlight the BPs connecting the **T** station with the **CB[7]** while panel d) the BPs between the **V** chemical moiety and the **CB[7]**, respectively. By coupling the information in Table 1 with that displayed in Figure 3 it should be quite simple to identify both the nature of the interaction patterns as well as its directionality. The AIM indices computed for the various BCPs, reported in Table 1, clearly unravel thenon-covalent nature of any contact occurring between the **T** and **V** stations with the surrounding macrocycle. As a matter of fact, at any BCP the $\rho(r)$ is within 0.017 $e{\cdot}a_0^{-3}$, the $\nabla^2\rho(r)$ and the $H(\mathbf{r})$ are positive, and the $-G(r)/V(r)$ ratio results greater than one. The only exception is represented by an interaction pattern connecting a hydrogen atom of the C_6H_5 ring of the **T** station with an oxygen atom of a C=O group located on the **CB[7]** (BCP = 405 in Table 1 and Figure 3c). Although rather weak, this interaction features a relatively small percentage of covalent character as indicated by the negative value of the $H(r)$ term and of the $-G(r)/V(r)$ ratio. Our data also indicate that: *i)* the methyl end-group of the **T** station can interact favorably with the proximal C=O crown of the **CB[7]** through seven intermolecular interactions (in Figure 3b) with DFT indicators explicitly reported in Table 1; *ii)* the same number of van der Waals contacts is appreciated for the C_6H_5 subunit with two BPs (230 and 327) also involving N atoms of the macrocycle and one BP (386) an aromatic C atom in interaction with a carbonyl O atom (see Figure 3c). These contacts arising from the crystallographic structure were never hypothesized before and actually are expected to play a not negligible contribution for allowing the presence of the **CB[7]** over **T** station. At last, such a mutual position is also reinforced by three C–H—O=C non-covalent interactions between a half moiety of the **V** station (that is the portion covalently bound to **T** station) and the macrocycle, see Figure 3d; these contacts span interatomic distances between 3.22 and 2.12 Å. Interestingly, we also observe that, the appreciated intermolecular contacts involving **T** and **V** stations are those undergoing a valuable shift in the ^{1}H NMR spectrum (termed as H_x and H_y) of **T-VPI** and **T-VPI-H$^+$** as a response to host:guest complexation; a ~0.7 and 0.9 ppm upfield shifts of H_x and H_y were observed in water at 300 K as a response of the complexation over the **T** station in the **T-VPI-H$^+$** thread.[28] We estimate from the X-ray structure an upfield shift – on average – of 1.4 ppm. The asymmetric interaction of **CB[7]** on hydrophobic groups like for instance tolyl or phenylene in molecular wires functionalized with charged and/or polar stations has intrigued several scientists in recent years as it is a non-trivial behaviour to be rationalized.[29,43] In this particular case,[28] it has been proposed that the presence of the **CB[7]** over the **T** station is essentially driven by the formation of strong charge assisted N$^+$C–H–O=C hydrogen bonds along the **CB[7]·V** border interface. From a purely geometrical point of view, these contacts are supposed to be less orthogonal (thus more stabilizing) with respect to a conformational shaping in which the macrocycle is superimposed over the **V** station itself. Our results depicted in Figure 3 and Table 1 support this observation while providing a more comprehensive picture - based on a DFT approach - of the non-covalent forces acting in this supramolecular context.

3.2. Identifying Non-Covalent Interactions in T-VPI(:CB[7]:)-Ag$^+$ Host:Guest Complex

Non-covalent interactions characterizing the **T-VPI(:CB[7]:)-Ag$^+$** host:guest complex are also addressed within the DFT-based proposed simulation scenario and the results of our computational analysis are reported in Table 2 and in Figure 4. At first, we focused our analysis on the nature of the chemical interactions allowing the complexation between the molecular shuttle and the silver cation. The coordination sphere is characterized by two short range contacts featuring interatomic distances confined within 2.42 Å and values of the $\rho(r)$ at the BCPs of ~0.040 (with the O atom of the ordered crystallographic water molecule)[28] and ~0.068 $e{\cdot}a_0^{-3}$ (with the N atom of the **I** station). Moreover, as further detailed in section 3.3, a negative value of the associated $H(\mathbf{r})$ at the BCPs should support the covalent nature of these two local interactions. In addition, we also characterized the peculiar features of the other contacts involved in the coordination sphere of the Ag^+ (see also Figure 4b): *i)* three non-covalent interactions are established with carbonyl O atoms at 2.70, 2.82, 2.87 Å distances, respectively. The $\rho(r)$ values are estimated in the 0.045–0.015 $e{\cdot}a_0^{-3}$ range and either the $\nabla^2\rho(r)$ or the $H(\mathbf{r})$ assumes positive value with a $-G(r)/V(r)$ ratio greater than one; *ii)* an unpredicted stabilizing interaction pattern also involve an H atom over the **P** station at 2.69 Å from the metal cation (see data reported in Table 2). As a next step, we extended our AIM-based investigation to other stations over the molecular thread. The X-ray crystallographic structure shows that the **CB[7]** preferentially surrounds the **P** and **I** stations with partial involvement also of the **V** one. Our analysis reveals that all these stations unequivocally form NCIs with the macrocycle. The **P** station, mainly at the center of this segment, presents 6 CPs (i.e., 240, 241, 242, 252, 359, 388 and 390) connecting polar C–H moieties with O or N atoms in the **CB[7]** as displayed in Figure 4b. A similar interacting pattern is found considering the intermolecular **V** and **CB[7]** couple in the **T-VPI(:CB[7]:)Ag$^+$(H$_2$O)** host:guest complex. As a matter of fact, when such a couple is concerned, our investigation shows the existence of 4 BPs (i.e., 270, 292, 358 and 362 in Figure 4c) connecting polar C–H groups in supramolecular interaction with carbonyl O atoms of the **CB[7]**. Furthermore, in this specific case we also identify other 4 supramolecular contacts between positive C atoms of the six-membered ring of a portion of the **V** station - as clearly shown from the ESP map in Figure 1 - and O atoms of the encircling macrocycle. We are referring to weak van der Waals interactions (termed as 269, 303, 353 and 373 in Table 2) with the entity of a supramolecular interaction finely modulated by inter-moiety distances. At last, as it can be seen in Figure 4d, a fraction of the **I** station substantially forms: *i)* 2 H-bonding contacts (367 and 369 in Table 2) with the polar N–H chemical

Table 2. Electron density $\rho(\boldsymbol{r})$ ($e{\cdot}a_0^{-3}$), Laplacian of electron density $\nabla^2\rho(\boldsymbol{r})$ ($e{\cdot}a_0^{-5}$), electron kinetic energy density $G(\boldsymbol{r})$ (hartree$\cdot a_0^{-3}$), electron potential energy density $V(\boldsymbol{r})$ (hartree$\cdot a_0^{-3}$), and electron energy density $H(\mathbf{r})$ (hartree$\cdot a_0^{-3}$) for bond critical points on selected bonds of the **T-VPI(:CB[7]:)Ag^+(H_2O)** molecular shuttle calculated at B3LYP(D3)/VTZ level of theory from the crystallographic structure (CCDC number 2217466).[28]

BCP [a]	Distance (in Å)	$\rho(\boldsymbol{r})$	$\nabla^2\rho(\boldsymbol{r})$	$G(\boldsymbol{r})$	$V(\boldsymbol{r})$	$-G(\boldsymbol{r})/V(\boldsymbol{r})$	$H(\mathbf{r})$
219[Ag^+-O70]	2.70	0.045361	0.224940	0.055532	−0.054842	1.012582	0.000690
222[Ag^+-Ow186]	2.42	0.040334	0.184889	0.046596	−0.046973	0.991974	−0.000377
227[Ag^+-O75]	2.87	0.014693	0.052592	0.012865	−0.012582	1.022492	0.000283
248[Ag^+-O68]	2.82	0.017011	0.060656	0.015089	−0.015015	1.004928	0.000074
253[Ag^+-H136]	2.69	0.010714	0.036152	0.007481	−0.005923	1.263042	0.001558
258[Ag^+-N87]	2.24	0.068635	0.301434	0.080894	−0.086452	0.935710	−0.005558
240[H137-N48]	2.99	0.003986	0.013576	0.002665	−0.001936	1.376550	0.000729
241[H136-O75]	2.48	0.008907	0.032328	0.006722	−0.005362	1.253637	0.001360
242[H137-N42]	2.95	0.004232	0.013583	0.002703	−0.002010	1.344776	0.000693
252[H137-O67]	2.94	0.003938	0.015062	0.002859	−0.001952	1.464652	0.000907
359[H135-O78]	3.22	0.002873	0.009753	0.001855	−0.001271	1.459481	0.000584
388[H138-O83]	2.36	0.011114	0.048441	0.009633	−0.007156	1.346143	0.002477
390[H135-O76]	2.86	0.004692	0.017673	0.003238	−0.002057	1.574137	0.001181
269[C101-O67]	3.44	0.003405	0.013690	0.002711	−0.001999	1.356178	0.000712
270[H123-O69]	2.49	0.008486	0.033875	0.006842	−0.005215	1.311985	0.001627
292[H123-O79]	3.13	0.001934	0.007754	0.001333	−0.000728	1.831044	0.000605
303[C105-O74]	3.36	0.004408	0.015983	0.003167	−0.002338	1.354577	0.000829
353[C101-O81]	3.76	0.001554	0.006423	0.001182	−0.000762	1.551181	0.000420
358[H130-O84]	2.51	0.007772	0.030816	0.006191	−0.004679	1.323146	0.001512
362[H126-O84]	2.86	0.003675	0.015496	0.002948	−0.002022	1.457962	0.000926
373[C105-O83]	3.23	0.005023	0.017779	0.003606	−0.002765	1.304159	0.000841
296[C86-O73]	3.23	0.005743	0.022053	0.004576	−0.003640	1.257143	0.000936
335[C86-O78]	3.74	0.001817	0.007408	0.001350	−0.000849	1.590106	0.000501
367[H120-O72]	2.01	0.021265	0.069136	0.016125	−0.014966	1.077442	0.001159
379[H120-O76]	2.83	0.003893	0.017622	0.003471	−0.002536	1.368691	0.000935

[a] BCP: from 219 to 258 involve Ag^+(185) ion in interaction with the **CB[7]**, the Imidazole (**I**), the Phenylene (**P**) station and a water molecule; from 240 to 390 the atoms constituting the Phenylene (**P**) station in interaction with the **CB[7]** and the Ag^+ ion; from 269 to 373 the half unit of the Viologen (**V**) group, covalently bonded to **P**, in supramolecular contact with the **CB[7]**; from 296 to 379 the bonding path connecting the Imidazole (**I**) unit with the **CB[7]**.

group of such a station in interaction with two different **CB[7]** carbonyl groups; *ii)* two further supramolecular contacts involving the carbon atom between the nitrogen atoms with two apical carbonyl groups at 3.23 and 3.74 Å (see Figure 4d and data in Table 2). It is therefore clear that the results herein reported provide an accurate description of the NCIs characterizing the binding motifs of the **CB[7]** macrocycle along the **T-VPI-Ag^+** molecular thread in the recently deposited X-ray crystallographic structure.[28] Finally, as already observed at the end of the subsection 3.1, we would like to remark that: *i)* the derived NCIs in Figure 4 and Table 2 involves interatomic couples that reflect changes in the ^{1}H-NMR spectra upon supramolecular complexation[28]; *ii)* the same computations applying a first principles hybrid functional (PBE0)[44] provide essentially the same patterns of non-covalent interactions and values for the QTAIM properties at the BCPs for the two supramolecular aggregates quite similar of those appreciated using the semi-empirical B3LYP one (see data in Table S1 and S2 in the Supporting Information); *iii)* we estimated a value of the complexation energy equal to −118.54 kcal/mol for the **CB[7]:T-VPI-H^+** and of −187.93 kcal/mol for the **T-VPI(:CB[7]:)-Ag^+**. These estimations, although not conclusive, highlight the preferential binding site for the **CB[7]** macrocycle when the molecular thread undergoes an electrophilic attack on the nitrogen atom of the **I**midazole moiety.

3.3. Local Electronic Energy Density - *H(r)* - Plots for an Ag^+ in a Molecular Shuttle

As a conclusive step, we further investigated the chemical interactions connecting the silver cation with the molecular shuttle on the basis of the X-ray crystal structure;[28] for the sake of completeness, also in this analysis we considered the ordered water molecules at 2.42 Å from the Ag^+ species in our modeling. To this end, the topology of the *H(r)* function in the framework of the AIM theory is analyzed over a plane defined by the nitrogen atom of the **I** station, the Ag^+ itself and the

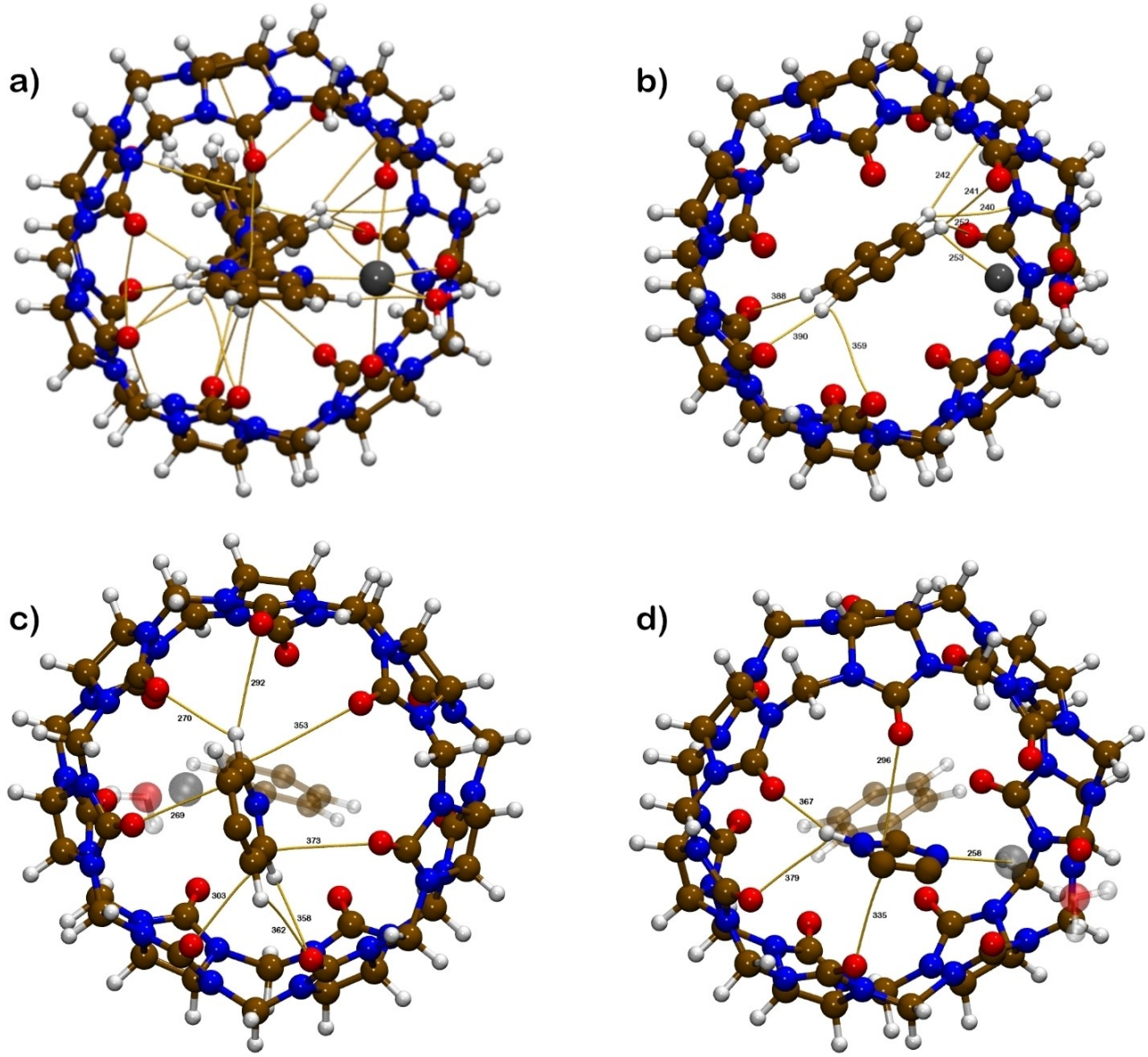

Figure 4. a) Non covalent bond paths – at B3LYP(D3)/VTZ level of theory – for the **T-VPI(:CB[7]:)Ag$^+$(H$_2$O)** molecular shuttle starting from X-ray crystallographic structure; bond paths connecting the **CB[7]** with the **P** station (b), a portion of the **V** station close to **P** (c) and a portion of the **I** station (d). The labels used for identifying the bond paths within the AIM workflow are those reported in Table 2.

oxygen atom of the water molecule [i.e., *H(**r**)* over σ(N87-Ag$^+$-Ow186)]. In this respect, the *H(**r**)* generally partitions the atomic space into inner regions of negative values, indicated as *H$^-$(**r**)*, and outer regions of positive values, indicated as *H$^+$(**r**)*. When two atoms form a chemical bond, their *H$^-$(**r**)* and *H$^+$(**r**)* regions combine in modes that properly signal the nature of the interaction.[45] In Figure 5 (upper panel) we report the plot of the *H(**r**)* function over the σ(N87-Ag$^+$-Ow186) plane. This picture clearly shows that, in the investigated framework the Ag$^+$ species is covalently bound to the N atom of the **I** station; there are no other covalent interactions in the first coordination sphere. In covalent interactions, the atoms overlap all the contour lines of their *H$^+$(**r**)* regions, and part of the contour lines of their inner *H$^-$(**r**)* regions, the bond appearing as a continuous region of negative values of *H(**r**)*, dived in a zone of positive values [i.e., *H$^+$(**r**)*]. In this specific case, it is clear that the negative value of the *H(**r**)* = –0.005558 hartree·a$_0^{-3}$ at the BCP along the Ag$^+$–N(**I**) path (see Table 2) coupled with the trend displayed in the upper panel of Figure 5 let us plausibly suppose the existence of a covalent-based interaction between these atoms. Such an interaction is expected to play a key role in driving the attachment of the Ag$^+$ cations over the **T-VPI** molecular threads after the addition of $AgNO_3$ in aqueous environment.[28] On the other hand, considering the Ag$^+$–Ow interacting couple, we would like to underline that even if the value of *H(**r**)* is negative at the BCP (i.e., –0.000377 hartree·a$_0^{-3}$ as reported in Table 2) there is no underlying covalent contact. It is worth noting that the value of the *H(**r**)* at the BCP is less

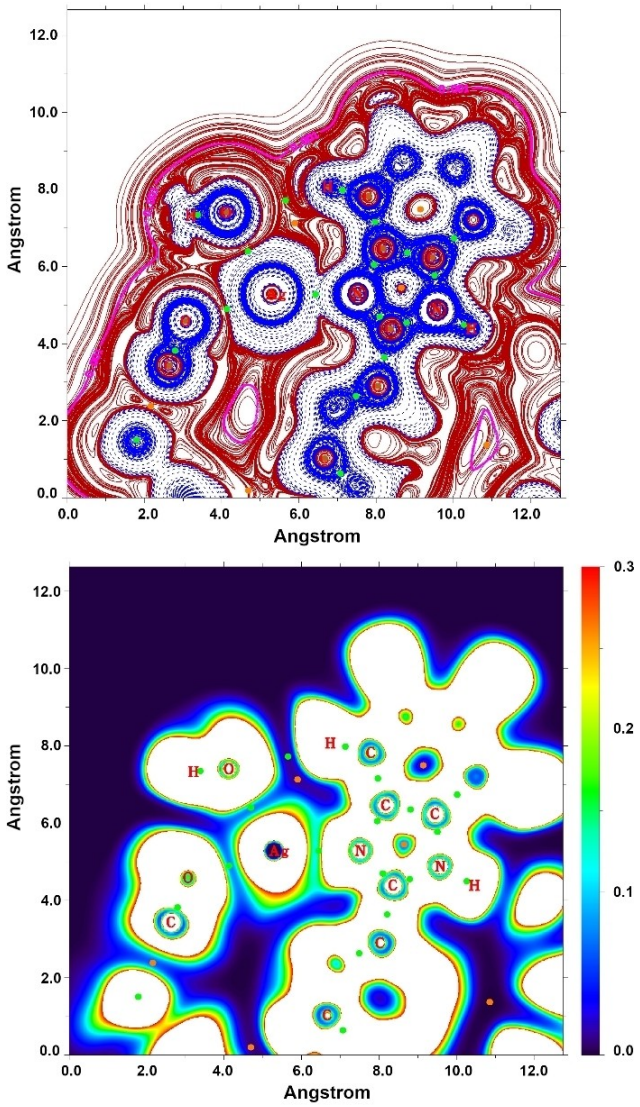

Figure 5. Upper panel: 2D-plots of the B3LYP(D3)/VTZ *H(r)* in the σ plane defined by the position of N87-Ag^+-Ow186 atoms in the X-ray structure.[28] The Ow186 is located approximately at the coordinate point (X = 4.2;Y = 7.5). Solid/brown and dashed/blue lines correspond, respectively, to positive and negative values. The green dots indicate the CPs (+3,–1) along the predefined bond paths (see also Figure 4 and data summarized in Table 2); CPs (+3,+1) are reported using orange dots. Lower panel: ELF map in the range 0.0–0.3 over the same plane as reported in the upper panel; white regions have ELF value larger than the upper limit of the color bar.

negative by an order of magnitude when compared to that between Ag^+–N(**I**); the plot of the *H(r)* shows that, at the BCP, Ag^+ and Ow overlap only part of their $H^+(r)$ regions, while their $H^-(r)$ regions remain closed and separated by a region of positive values of *H(r)*. This is a typical example of weak non-covalent contacts of variable nature. Always remaining in this context, we realize that weaker supramolecular interactions also involve carbonyl oxygen atoms of the **CB[7]** belonging to the first coordination sphere of the Ag^+ cation (see data collected in Table 2). This aspect might actually explain the shuttling mechanism experimentally observed when the **CB[7]** macrocycle encircles the **T-VPI-Ag$^+$** molecular thread[28]; this basically because the formation of covalent contacts and/or of strong van der Waals interactions between the silver cation and the macrocycle would have not allowed the reversible shuttling among **T** and **P** stations of the latter. Moreover, this analysis is further supported by the Electron Localization Function (ELF) plot - between 0.0 and 0.3 - reported in the lower panel of Figure 5. A graphical representation of the ELF is able to give a qualitative picture of the type of bonds in a molecular system and the regions of the space where it is possible to find electron pairs. In this respect, looking at the ELF sampled values over the σ(N87-Ag^+-Ow186) plane, it is evident to assume that the Ag^+ features a partially covalent connection with the lone pairs of the N atom of the **I** station. At the BCP connecting Ag^+ and N, the ELF samples value at around 0.20; on the contrary, the same value results substantially lower (< 0.05) both for the Ag^+–Ow and Ag^+–O=C(**CB[7]**) interactions. This graphical representation well highlights the differences between covalent and non-covalent coordination sites for the silver cation in the X-ray structure of the currently investigated molecular shuttle.

4. Conclusions

In this contribution we theoretically investigate a recently released pH- and Metal-Actuated molecular shuttle with the target of unravelling the supramolecular interacting patterns finely modulating the mutual position of **CB[7]** macrocycles along **T-VPI-H$^+$** and **T-VPI-Ag$^+$** molecular threads. The results that have emerged, considering the X-ray molecular structure of **T-VPI-Ag$^+$** available in literature, highlight that a large reservoir of non-covalent interactions work in a cooperative way for stabilizing the host(**CB[7]**):guest(**T-VPI-Ag$^+$**) shuttle with a ratio of 2:1. Moreover the results herein reported estimating QTAIM descriptors from DFT converged wavefunctions are consistent with the experimentally observed reversible shuttling process of the **CB[7]** macrocycle when in interaction with the **T-VPI-Ag$^+$** system. This contribution then shows that computational methodologies may become an excellent tool to support laboratory experiments for a rational design of highly complex molecular machines and devices. At last, we believe that it would be useful to address two further intriguing points in the next future. First, the methodology proposed in this study might be extended over an ensemble of statistically relevant conformations of such a molecular shuttle in explicit water solution coupling electronic degrees of freedom with classical molecular dynamics propagators. Second, this study did not explore from a computational viewpoint the potential applications of other cations. In this respect, it might be interesting to explore the effect of replacing Ag^+ with other metal species that could potentially also inhibit the dynamics of the **CB[7]** macrocycle.

Acknowledgements

This study is supported by the Rome Technopole foundation within the PNRR action in the field of the NextGenerationEU –

section 4. "Digital, Industry and Aerospace". We thank the University of Tuscia for having allowed the utilization of the DIBAF Cluster HPC Infrastructure where all the computations were carried out. Open Access publishing facilitated by Università degli Studi della Tuscia, as part of the Wiley - CRUI-CARE agreement.

Conflict of Interests

The authors declare no conflict of interest.

Data Availability Statement

The data that support the findings of this study are available from the corresponding author upon reasonable request.

Keywords: Nanoscale devices · Molecular shuttles · Cucurbituril · Quantum Theory of Atoms in Molecules · Density Functional Theory

[1] J.-M. Lehn, *Supramolecular chemistry: concepts and perspectives*, Wiley-VCH, Weinheim **1995**.
[2] V. Balzani, A. Credi, M. Venturi, *M. Molecular Machines and Devices: Concepts and Perspectives for the Nanoworld*, Wiley-VCH, Weinheim, Germany **2008**.
[3] R. A. L. Jones, *Soft Machines, Nanotechnology and Life*, Oxford University Press, Oxford, U. K. **2004**.
[4] J. F. Stoddart, *Chem. Soc. Rev.* **2009**, *38*, 1802.
[5] B. Feringa, *Nature* **2000**, *408*, 151.
[6] S. Silvi, A. Credi, *A. In Nanotechnology for Biology and Medicine*, Springer: New York **2012**, 71–100.
[7] S. Saha, J. F. Stoddart, Molecular Motors and Muscles*, in Functional Organic Materials: Syntheses, Strategies and Applications*, (Eds: T. J. J. Müller, U. H. F. Bunz), Wiley-VCH Verlag GmbH & Co. KGaA **2007**.
[8] J. F. Stoddart, *Angew. Chem., Int. Ed.* **2017**, *56*, 11094.
[9] J.-P. Sauvage, *Angew. Chem., Int. Ed.* **2017**, *56*, 11080.
[10] B. L. Feringa, *Angew. Chem., Int. Ed.* **2017**, *56*, 11060.
[11] S. Kassem, T. van Leeuwen, A. S. Lubbe, M. R. Wilson, B. L. Feringa, D. A. Leigh, *Chem. Soc. Rev.* **2017**, *46*, 2592.
[12] M. Baroncini, L. Casimiro, C. De Vet, J. Groppi, S. Silvi, A. Credi, *ChemistryOpen* **2018**, *7*, 169.
[13] I. Aprahamian, *ACS Cent. Sci.* **2020**, *6*, 347.
[14] V. Balzani, A. Credi, M. Venturi, *NanoToday* **2007**, *2*, 18, and quoted references therein cited.
[15] a) A. M. Brouwer, C. Frochot, F. G. Gatti, D. A. Leigh, L. Mottier, F. Paolucci, S. Roffia, W. H. Wurpel, *Science* **2001**, *291*, 2124; b) A. Altieri, F. G. Gatti, E. R. Kay, D. A. Leigh, D. Martel, F. Paolucci, A. M. Z. Slawin, J. K. Y. Wong, *J. Am. Chem. Soc.* **2003**, *125*, 8644–8654.
[16] a) C. Zazza, A. Amadei, N. Sanna, M. Aschi, *Chem. Commun.* **2008**, *29*, 3399–3401; b) M. Kimura, T. Mizuno, M. Ueda, S. Miyagawa, T. Kawasaki, Y. Tokunaga, *Chem. Asian J.* **2017**, *12*, 1381–1390; c) M. Ueda, S. Terazawa, Y. Deguchi, M. Kimura, N. Matsubara, S. Miyagawa, T. Kawasaki, Y. Tokunaga, *Chem. Asian J.* **2016**, *11*, 2291–2300.
[17] a) P. Roy, W. R. Browne, B. L. Feringa, S. R. Meech, *Nature Comm.* **2023**, *14*, 1253; b) W. Danowski, T. van Leeuwen, S. Abdolahzadeh, D. Roke, W. R. Browne, S. J. Wezenberg, B. Feringa, *Nat. Nanotechnol.* **2019**, *14*, 488–494.
[18] a) C. Zazza, S. Borocci, N. Sanna, *Phys. Chem. Chem. Phys.* **2024**, *26*, 5399–5407; b) P. Liu, C. Chipot, X. Shao, W. Cai, *J. Phys. Chem. C* **2012**, *116*, 4471–4476; c) L. Leanza, C. Perego, L. Pesce, M. Salvalaglio, M. von Delius, G. M. Pavan, *Chem. Sci.* **2023**, *14*, 6716–6729.
[19] a) D.-H. Qu, B. Feringa, *Angew. Chem., Int. Ed.* **2010**, *49*, 1107–1110; b) N. N. Bach, V. Josef, H. Maid, H. Dube, *Angew. Chem.* **2022**, *134*, e202201882; c) J. Sheng, W. Danowski, A. S. Sardjan, J. Hou, S. Crespi, A. Ryabchun, M. Paradiz Domínguez, W. J. Buma, W. R. Browne, B. Feringa, *Nat. Chem.* **2024**, DOI: 10.1038/s41557-024-01521-0.
[20] a) C. Zazza, G. Mancini, G. Brancato, V. Barone, *J. Phys. Chem. Lett.* **2013**, *4*, 3885–3890; b) Jos C. M. Arjen Cnossen, Tatsuo Kojima Kistemaker, Ben L. Feringa, *J. Org. Chem.* **2014**, *79*, 927–935; c) Z. Wu, S. Wang, Z. Zhang, Y. Zhang, Y. Yin, H. Shi, S. Jiao, *RSC Adv.* **2022**, *12*, 30495–30500; d) H. Fu, X. Shao, C. Chipot, W. Cai, *Chem. Sci.* **2017**, *8*, 5087–5094.
[21] a) K. Kuntze, D. R. S. Pooler, M. Di Donato, M. F. Hilbers, P. Van Der Mulen, W. J. Buma, A. Priimagi, B. Feringa, S. Crespi, *Chem. Sci.* **2023**, *14*, 8458–8465; b) P. Roy, A. S. Sardjan, W. R. Browne, B. L. Feringa, S. R. Meech, *J. Am. Chem. Soc.* **2024**, *146*, 12255–12270.
[22] a) C. Zazza, S. Borocci, N. Sanna, F. Grandinetti, *Chem. Phys. Lett.* **2024**, *842*, 141205; b) B. Oruganti, J. Wang, B. Durbeej, *Org. Lett.* **2017**, *19*, 4818; c) M. Feng, M. K. Gilson, *Phys. Chem. Chem. Phys.* **2021**, *23*, 8525; d) H. Xu, B. Zhang, Y. Tao, W. Xu, B. Hu, F. Yan, J. Wen, *J. Phys. Chem. A* **2023**, *127*, 7682.
[23] a) G. Ragazzon, M. Baroncini, S. Silvi, M. Venturi, A. Credi, *Nat. Nanotech.* **2014**, *10*, 70; b) S. Corra, M. Curcio, A. Credi, *JACS Au* **2023**, *3*, 1301–1313; c) K. Zhu, G. Baggi, S. J. Loeb, *Nat. Chem.* **2018**, *10*, 625–630.
[24] a) C. Zazza, S. Borocci, N. Sanna, *Chem. Phys. Lett.* **2023**, *829*, 140758;' b) J. Lv, Y. Ding, P. Sun, J. Wang, T. Chen, X. Zhao, C. Fang, L. Wang, *Chem. Phys. Lett.* **2023**, *811*, 140245; c) A. Nikiforov, J. A. Gamez, W. Thiel, M. Filatov, *J. Phys. Chem. Lett.* **2016**, *7*, 105–110.
[25] a) S. Zhang, Y. An, X.-M. Chen, Q. Li, *Smart Molecules* **2023**, *1*, e20230015; b) S. Garaudée, S. Silvi, M. Venturi, A. Credi, A. H. Flood, J. F. Stoddart, *ChemPhysChem* **2005**, *6*, 2145–2152; c) G. Ragazzon, A. Credi, B. Colasson, *Chem. Eur. J.* **2017**, *23*, 2149–2156; d) N. Farahani, K. Zhu, S. J. Loeb, *ChemPhysChem* **2016**, *17*, 1875–1880; e) S. Kozáková, N. Alharzali, I. Černušák, *Phys. Chem. Chem. Phys.* **2023**, *25*, 29386–29403; f) K. Asai, Q. Mao, A. Nakagami, H. Kitagishi, *Eur. J. Org. Chem.*, **2024**, 27, e202400081; g) A. Singhania, S. Kalita, P. Chettri, S. Ghosh, *Nanoscale Adv.* **2023**, *5*, 3177–3208.
[26] P. L. Anelli, N. Spencer, J. F. Stoddart, *J. Am. Chem. Soc.* **1991**, *113*, 5131.
[27] R. A. Bissell, E. Cordova, A. E. Kaifer, J. F. Stoddart, *Nature* **1994**, *369*, 133.
[28] A. Kriat, S. Pascal, B. Kauffmann, Y. Ferrand, D. Bergè-Lefranc, D. Gigmes, O. Siri, A. Kermagoret, D. Bardelang, *Chem. Eur. J.* **2023**, *29*, e202300633.
[29] a) Q. Cheng, H. Yin, R. Rosas, D. Gigmes, O. Ouari, R. Wang, A. Kermagoret, D. Bardelang, *Chem. Commun.* **2018**, *54*, 13825; b) H. Yin, R. Rosas, D. Gigmes, O. Ouari, R. Wang, A. Kermagoret, D. Bardelang, *Org. Lett.* **2018**, *20*, 3187; c) A. Kermagoret, David Bardelang, *Chem. Eur. J.* **2023**, *29*, e202302114.
[30] a) R. F. W. Bader, *Chem. Rev.* **1991**, *91*, 893. b) R. F. W. Bader, in *Atoms in Molecules: A Quantum Theory*, Oxford University Press, Oxford **1990**. c) F. Cortés-Guzmán, J. I. Rodríguez, and J. S. M. Anderson, in *Advances in Quantum Chemical Topology Beyond QTAIM*, (Eds: J. I. Rodríguez, F. Cortés-Guzmán, J. S. M. Anderson), Elsevier Inc. **2023**, 1-19.
[31] W. Koch, M. C. Holthausen, *A Chemist's Guide to Density Functional Theory*, 2nd Edition, Wiley-VCH Verlag GmbH, **2001**.
[32] a) A. D. Becke, *Phys. Rev. A* **1988**, *38*, 3098; b) C. Lee, W. Yang, R. G. Parr, *Phys. Rev. B* **1988**, *37*, 785; c) S. H. Vosko, L. Wilk, M. Nusair, *Can. J. Phys.* **1980**, *58*, 1200.
[33] T. H. Dunning Jr., *J. Chem. Phys.* **1989**, *90*, 1007–1023.
[34] S. Grimme, J. Antony, S. Ehrlich, H. Krieg, *J. Chem. Phys.* **2010**, *132*, 154104.
[35] G. Saleh, C. Gatti, L. Lo Presti, *Comput. Theor. Chem.* **2015**, *1053*, 53–59.
[36] a) E. R. Johnson, S. Keinan, P. Mori-Sanchez, J. Contreras-Garcia, A. J. Cohen, W. Yang, *J. Am. Chem. Soc.* **2010**, *132*, 6498; b) C. Narth, Z. Maroun, R. A. Boto, R. Chaudret, M. L. Bonnet, J.-P. Piquemal, J. Contreras-García, A complete NCI perspective: from new bonds to reactivity, *in Applications of Topological Methods in Molecular Chemistry*, (Eds: R. Chauvin, C. Lepetit, B. Silvi, E. Alikhani), Springer **2016**, *22*, 491–527.
[37] T. Lu, F. Chen, *J. Comput. Chem.* **2012**, *33*, 580.
[38] Gaussian 16, Revision C.01, M. J. Frisch, G. W. Trucks, H. B. Schlegel, G. E. Scuseria, M. A. Robb, J. R. Cheeseman, G. Scalmani, V. Barone, G. A. Petersson, H. Nakatsuji, X. Li, M. Caricato, A. V. Marenich, J. Bloino, B. G. Janesko, R. Gomperts, B. Mennucci, H. P. Hratchian, J. V. Ortiz, A. F. Izmaylov, J. L. Sonnenberg, D. Williams-Young, F. Ding, F. Lipparini, F. Egidi, J. Goings, B. Peng, A. Petrone, T. Henderson, D. Ranasinghe, V. G. Zakrzewski, J. Gao, N. Rega, G. Zheng, W. Liang, M. Hada, M. Ehara, K. Toyota, R. Fukuda, J. Hasegawa, M. Ishida, T. Nakajima, Y. Honda, O. Kitao, H. Nakai, T. Vreven, K. Throssell, J. A. Montgomery, Jr., J. E. Peralta, F. Ogliaro, M. J. Bearpark, J. J. Heyd, E. N. Brothers, K. N. Kudin, V. N. Staroverov, T. A. Keith, R. Kobayashi, J. Normand, K. Raghavachari, A. P. Rendell, J. C. Burant, S. S. Iyengar, J. Tomasi, M. Cossi, J. M. Millam, M.

Klene, C. Adamo, R. Cammi, J. W. Ochterski, R. L. Martin, K. Morokuma, O. Farkas, J. B. Foresman, and D. J. Fox, Gaussian, Inc., Wallingford CT **2016**.
[39] S. Armaković, S. J. Armaković, *Mol. Simul.* **2023**, *49*, 117–123.
[40] W. Humphrey, A. Dalke, K. Schulten, *J. Mol. Graph.* **1996**, *14*, 33.
[41] J. Zhang, T. Lu, *Phys. Chem. Chem. Phys.* **2021**, *23*, 20323.
[42] M. Cossi, N. Rega, N. G. Scalmani, V. Barone, *J. Comput. Chem.* **2003**, *24*, 669.
[43] a) V. Sindelar, S. Silvi, A. E. Kaifer, *Chem. Commun.* **2006**, 2185–2187; b) M. Freitag, L. Gundlach, P. Piotrowiak, E. Galoppini, *J. Am. Chem. Soc.* **2012**, *134*, 3358–3366; c) F. Benyettou, K. Nchimi-Nono, M. Jouiad, Y. Lalatonne, I. Milosevic, L. Motte, J.-C. Olsen, N. I. Saleh, A. Trabolsi, *Chem. Eur. J.* **2015**, *21*, 4607–4613; d) L. Zhu, H. Yan, X.-J. Wang, Y. Zhao, *J. Org. Chem.* **2012**, *77*, 10168–10175.
[44] C. Adamo, V. Barone, *J. Chem. Phys.* **1999**, *110*, 6158–6169.
[45] a) S. Borocci, P. Cecchi, F. Grandinetti, N. Sanna, C. Zazza, *Phys. Chem. Chem. Phys.* **2024**, *26*, 7377–7387; b) S. Borocci, F. Grandinetti, N. Sanna, C. Zazza, *Chem. Asian J.* **2024**, *19*, e202400191.

Manuscript received: May 31, 2024
Revised manuscript received: July 15, 2024
Accepted manuscript online: August 15, 2024
Version of record online: October 22, 2024